Artemis I Optical Navigation System Performance

Rebecca Inman[1] and Greg Holt[2]
NASA Johnson Space Center, Houston, TX 77058, USA

John Christian[3]
Georgia Institute of Technology, Atlanta, GA 30332, USA

Kyle Smith[4]
The Charles Stark Draper Laboratory, Houston, TX 77058, USA

Christopher D'Souza[5]
NASA Johnson Space Center, Houston, TX 77058, USA

This paper summarizes the assessment of the Optical Navigation Flight Test Objective (FTO) during the flight of Artemis I. The Optical Navigation (OpNav) System was tested under a variety of range, target, and lighting conditions to evaluate the performance compared to the pre-flight predicted error models. In general, OpNav performed very well – successfully processing over a thousand images of starfields, Earth, and Moon. The performance of the algorithm when processing Moon images matched the pre-flight expected error models. The errors when processing Earth images were notably higher than the pre-flight models predicted, however this was found to be due to an over-estimation of the atmosphere bias used in the tuning of the algorithm. After the bias was re-tuned and the images reprocessed, performance significantly improved.

I. Introduction

The Orion Optical Navigation (OpNav) system's primary purpose is to serve as a backup source of Position/Velocity navigation state information for should the vehicle experience a Permanent Communication Loss (PCL). Using an image of the Earth or Moon, the relative position (i.e. range and bearing) to the observed celestial body can be estimated with observations of the lit limb. Although there is a long and storied history of limb-based OpNav performed by human analysists on the Earth, a fully onboard and completely autonomous image processing algorithm of this type is believed to be the first of its kind.

Prior to the Artemis I flight, the OpNav performance was predicted based on simulated and ground images. While simulated images provide the basis for a performance assessment and error model development, they are not truly representative of real-world conditions as seen from a camera in space. This paper documents the performance of the Optical Navigation System during the Artemis I flight compared to the pre-flight error models (See [1] for a derivation of the error models, but note that the actual bias and noise values were changed slightly).

---

[1] Aerospace Engineer, EG6
[2] Orion Flight Dynamics Navigation Lead, EG6
[3] Associate Professor, Guggenheim School of Aerospace Engineering, AIAA Associate Fellow
[4] Senior Member Technical Staff
[5] NASA JSC Technical Fellow, NASA Langley Research Center, AIAA Fellow

In general, this analysis is dependent upon the quality of the Best Estimated Trajectory (BET) of the Orion vehicle during the Artemis I mission. OpNav was just one part of the overall Navigation System on Orion (see Ref [2]). Errors in the BET limit the accuracy of the performance assessment.

II. OpNav on Artemis I Flight

The Artemis I mission was the first in-flight demonstration of the Orion Optical Navigation system. For Orion, the primary purpose of OpNav is a back-up navigation sensor in the event of a loss of communication with the ground. Due to vehicle pointing constraints, OpNav could not be used continuously. Instead, OpNav was performed in "passes," where the vehicle was maneuvered to point at either the Earth or the Moon to collect a sequence of observations approximately once per day (i.e., once per 24 hours). Each pass was preceded by an in-flight calibration using starfield images to estimate camera parameters and the Star Tracker to OpNav Camera interlock angle.

Table 1 summarizes all the OpNav passes throughout the Artemis I flight. The passes consisted of the two Earth certification passes (one primary and one back-up), two Moon certification passes (one primary and one back-up), and several image gathering passes. The certification passes were approximately 2 hours each, with images taken every 30 seconds. The subsequent image gathering passes were 10 minutes each, taken at the same 30 second interval. In the event of a loss of communication, the image gather passes would have been converted to full 2-hour passes. Due to known large errors in the ground state update, Pass #16 (Earth) is not included in this analysis. Lastly, as noted in Table 1, two Moon image gathering passes are not included in this analysis due to incomplete data sets caused by telemetry issues.

Figures 1 and 2 show an example Earth and Moon image from the certification passes.

Table 1 OpNav Pass Details

Pass #	Target	~Range (nmi)	Notes
1	Earth	83600	Certification pass
2	Earth	113100	Back-up certification pass
3	Moon	136300	Certification pass
4	Moon	121000	Back-up certification pass
5	Moon	89300	Image gathering
6	Moon	51500	Image gathering
7	Moon	19000	Image gathering
8	Moon	19200	Image gathering
9	Moon	42900	Image gathering
10	Moon	49500	Image gathering
11	Moon	50800	Image gathering
12	Moon	46660	Image gathering
13	Moon	41100	Image gathering
14	Moon	44750	Image gathering
15	Moon	47500	Image gathering
16	Earth	204500	Image gathering – not used in this analysis
17	Moon	39600	Image gathering – not used in this analysis
18	Moon	27300	Image gathering
19	Moon	13060	Image gathering
20	Moon	37400	Image gathering
21	Moon	86900	Image gathering – not used in this analysis
22	Moon	147500	Image gathering
23	Earth	158000	Image gathering
24	Moon	207500	Image gathering
25	Earth	81500	Image gathering
26	Earth	52100	Image gathering

Fig. 1 Earth Certification Pass Image

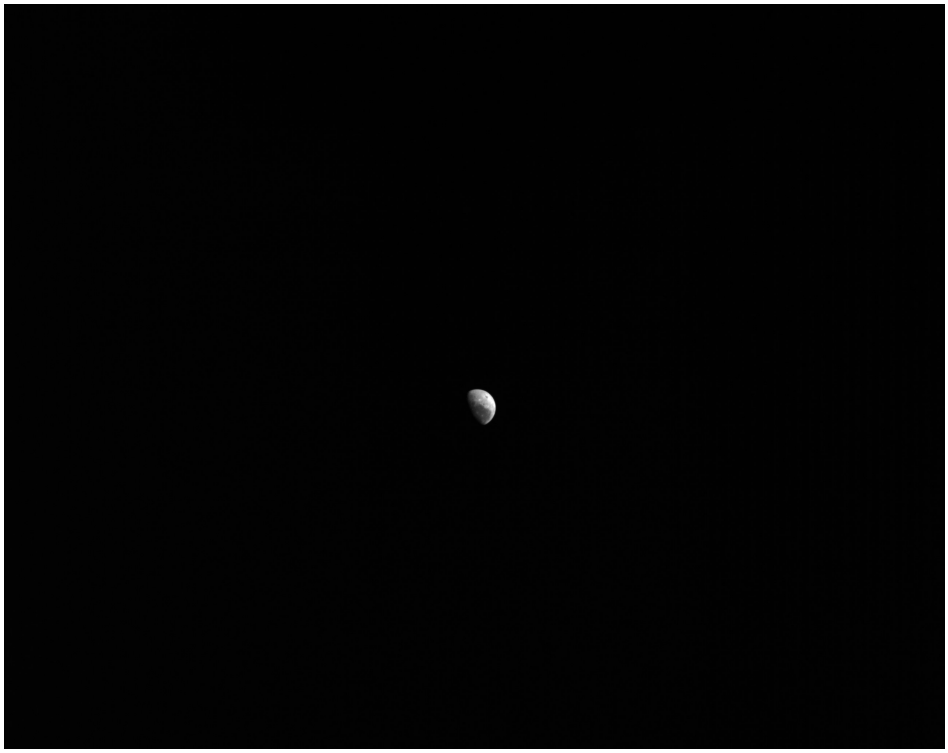

Fig. 2 Moon Certification Pass Image

III. OpNav System Overview

The Orion onboard OpNav system is a synthesis of image processing and navigation algorithms developed by university partners. We leverage both a non-iterative method and an iterative method to produce a relative position from the camera to the target body in the form of a range and bearing tangent angles.

A. Non-Iterative OpNav Algorithm

Orion's horizon-based OpNav system uses the Christian-Robinson algorithm (CRA) in the form described within Refs. [3] and [4]. As compared to other limb-based methos (e.g., limb-scanning [5], explicit ellipse fitting [6,7]), the primary advantages of the CRA are: (1) it exactly captures the geometry of the limb projection for an ellipsoidal body, (2) it is non-iterative and requires no initial guess, (3) it does not require a photometric model of the observed celestial body, and (4) it is substantially faster than alternative approaches.

The CRA proceeds roughly as follows (see Ref. [3] for a detailed derivation). Given an image with the Earth or Moon, we scan the image in the direction of incoming sunlight to find pixel-level estimates of the lit limb's location [4]. Then, these pixel-level limb estimates are refined to have subpixel accuracy using the moment-based method of Refs. [4] and [8]. Let $\boldsymbol{u}_i = [u; v]$ be the non-integer pixel coordinates of a point observed on the body's lit limb as produced by the subpixel edge localization algorithm. We generally find it helpful to write these limb locations in homogeneous pixel coordinates as $\overline{\boldsymbol{u}}_i = [u; v; 1]$.

Suppose that we measure a set of n horizon points $\{\overline{\boldsymbol{u}}_i\}_{i=1}^n$ belonging to the apparent lit limb in an image. Assuming a calibrated camera (see §IV.A), these image points may be converted to homogeneous image plane coordinates $\{\overline{\boldsymbol{x}}_i\}_{i=1}^n$ using the standard relation

$$\overline{\boldsymbol{x}}_i = \boldsymbol{K}^{-1}\overline{\boldsymbol{u}}_i$$

where $\boldsymbol{K}$ is camera calibration matrix. We note that $\boldsymbol{K}^{-1}$ which may be computed analytically as discussed in Ref. [3].

The CRA works by transforming the image plane measurements $\{\overline{\boldsymbol{x}}_i\}_{i=1}^n$ into a space where any arbitrary ellipsoidal (celestial) body becomes a unit sphere. If we describe the celestial body's shape matrix in the camera frame as $\boldsymbol{A}_C$, then we seek the matrix decomposition $\boldsymbol{A}_C = \boldsymbol{B}^T\boldsymbol{B}$ to perform a transformation of the form $\boldsymbol{s}_i = \boldsymbol{B}\overline{\boldsymbol{x}}_i$. The matrix decomposition $\boldsymbol{A}_C = \boldsymbol{B}^T\boldsymbol{B}$ is not unique. Artemis I uses of the SVD version of this algorithm (as suggested in [3,4]) instead of the Cholesky version that appeared in the original paper describing the CRA [10].

Specifically, we use the SVD to write

$$\boldsymbol{A}_C = \boldsymbol{B}^T\boldsymbol{B} = \boldsymbol{T}_C^P\boldsymbol{A}_P\boldsymbol{T}_P^C$$

where $\boldsymbol{T}_P^C$ is the known rotation matrix from the OpNav camera frame to the planet's principal axis frame. Since $\boldsymbol{A}_P = \mathrm{diag}[a^{-2}, b^{-2}, c^{-2}]$ for a body with principal axes lengths $\{a, b, c\}$, we may write

$$\boldsymbol{A}_C = \boldsymbol{B}^T\boldsymbol{B} = \boldsymbol{T}_C^P\boldsymbol{D}\boldsymbol{D}\boldsymbol{T}_P^C = (\boldsymbol{D}\boldsymbol{T}_P^C)^T(\boldsymbol{D}\boldsymbol{T}_P^C)$$

where

$$\boldsymbol{D} = \mathrm{diag}[a^{-1}, b^{-1}, c^{-1}]$$

Consequently, we may directly write $\boldsymbol{B}$ in terms of the known matrices $\boldsymbol{D}$ and $\boldsymbol{T}_P^C$ without ever needing to explicitly perform any kind of decomposition in software. That is, we just write $\boldsymbol{B}$ directly as

$$\boldsymbol{B} = \boldsymbol{D}\boldsymbol{T}_P^C$$

Therefore, we proceed by transforming our image plane measurements $\{\overline{\boldsymbol{x}}_i\}_{i=1}^n$ according to the simple matrix multiplication with the known matrix $\boldsymbol{B}$

$$\boldsymbol{s}_i = \boldsymbol{B}\overline{\boldsymbol{x}}_i = \boldsymbol{D}\boldsymbol{T}_P^C\overline{\boldsymbol{x}}_i$$

We now take advantage of the fact that our transformation maps all ellipsoidal bodies to a unit sphere---thus allowing a least square solution by simple trigonometry. We first compute the unit vectors in the direction of $\boldsymbol{s}_i$ and denote it as $\boldsymbol{s}_i' = \boldsymbol{s}_i/\|\boldsymbol{s}_i\|$. We then compute the linear system for the vector $\boldsymbol{n}$ having an identical angle with each unit vector $\boldsymbol{s'}_i$. If the angle θ_i between these vectors is constant, then $\boldsymbol{n}^T\boldsymbol{s}_i' = \|\boldsymbol{n}\|\cos\theta_i = const$. Consequently, we may write

$$\begin{bmatrix} \boldsymbol{s}_1'^T \\ \vdots \\ \boldsymbol{s}_n'^T \end{bmatrix}\boldsymbol{n} = \begin{bmatrix} 1 \\ \vdots \\ 1 \end{bmatrix}$$

which may be solved for $\boldsymbol{n}$ in the least squares (or total least squares) sense.

Once n is known, we may directly recover the position of the observed celestial body relative to the camera (as expressed in the camera frame C) as

$$\boldsymbol{r}_C = (\boldsymbol{n}^T\boldsymbol{n} - 1)^{-1/2}\,\boldsymbol{T}_C^P\boldsymbol{D}^{-1}\boldsymbol{n}$$

where we note that $\boldsymbol{D}^{-1}$ is simply

$$\boldsymbol{D}^{-1} = \mathrm{diag}[a, b, c]$$

This allows for the direct and exact estimation of $\boldsymbol{r}_C$ from measured image points $\{\overline{\boldsymbol{u}}_i\}_{i=1}^n$ around the apparent lit horizon of an ellipsoidal celestial body.

B. Iterative OpNav Algorithm

In addition to the non-iterative OpNav algorithm (the CRA) discussed in §III.B, Artemis I also had an iterative algorithm based on work by Mortari, et al. [11]. Since this iterative algorithm requires an initial guess, we used the solution for the CRA as a starting point. The method of Mortari then proceeds by iteratively minimizing the residual between the image gradient around the lit limb with that of an ellipsoidal sigmoid function.

The algorithm will iterate until the update drops below a predefined threshold or until the maximum number of allowed iterations is reached. Typically, the algorithm will converge within 5-10 iterations.

IV. Results/Discussion

This section details the overall performance of the OpNav system during the Artemis I Flight. Earth and Moon performance are assessed separately, as each target has a unique error model.

The primary method to determine the Optical Navigation system performance was a comparison of the OpNav measurements to the onboard BET. The measurement errors are compared against the expected pre-flight error models. A characterization of the BET uncertainty is taken into account when analyzing the performance for the certification passes.

A. OpNav In-Flight Calibration

The OpNav system converts camera pixel locations into line-of-sight vectors in the camera frame using a camera model. The relative attitude between the camera and two Star Tracker (ST) sensors on Orion is also important. The camera model and relative sensor alignments are characterized on the ground before flight [12], but due to potential changes in sensor characteristics and orientations from the dynamics of launch, transition from atmosphere to vacuum, thermal effects, and other potential environmental factors, these values were also measured prior to each OpNav pass

using images of stars and onboard calibration software in an attempt to characterize the stability of the calibration throughout flight.

The calibration method implemented by the OpNav system uses star field images, along with associated attitudes derived from STs at the time of image capture, has been detailed previously [9]. Here we will only briefly mention that the calibration procedure identifies star centroids in the image, associates them with known catalog stars based on the estimated attitude, and performs a fit of the camera model using an iterative Levenberg-Marquardt algorithm.

During Artemis I, 30 calibrations were performed using 20 images of star fields for each calibration. Each set of star field images was acted on by the calibration software for three iterations to ensure convergence of the algorithm, resulting in 90 data points for each model parameter estimated in-flight. The results show that there was an initial shift in several model parameters between the ground calibration and the first in-flight calibration, but relative stability in model parameters over the duration of the mission.

Only one OpNav calibration attempt failed, which was due to a violation of model residual statistics acceptance criteria. Figure 3 is a composite of nine calibration images from the failed calibration attempt which shows a single star moving across the camera's field of view. In the fifth image, a cluster of bright pixels is observed nearby the star but does not appear in the previous or subsequent images. We conclude that this non-stellar object is most likely the result of a radiation strike on the detector. This cluster of pixels was falsely identified as a star resulting in a large associated residual in the fit model, which violated the calibration acceptance criteria. Updates in the calibration software for future missions have been made to reject such outliers, rather than fail the calibration, as was done here.

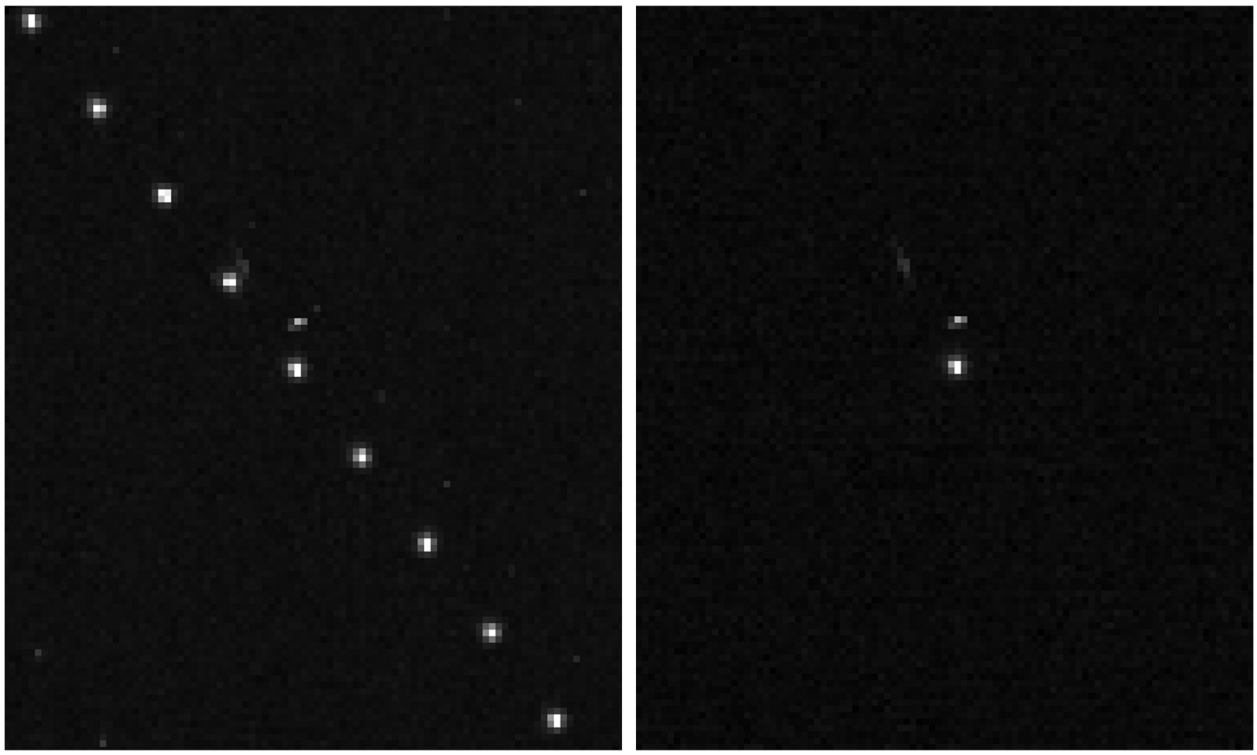

Fig. 3 Cropped composite of nine failed calibration images (left) and the cropped single image which resulted in calibration failure (right).

Orion OpNav uses the Brown-Conrady lens distortion model [13, 14] with five parameters (k_1, k_2, k_3, p_1, p_2) to transform between distorted (observed) and undistorted (ideal) image plane coordinates. The distorted image plane coordinates may be computed from the image pixel coordinates by a simple affine transformation containing another five parameters (*dx, dy, alpha,* u_p, v_p). The ideal image plane coordinates are related to the camera frame line-of-sight directions through a pinhole camera model.

As is common practice, the choice was made to leave the image principal point location (u_p, v_p) fixed at the center of the detector. The summary of the fit calibration results is shown in Fig. 4. The higher order radial distortion parameters k_2 and k_3 were observed to fluctuate significantly. Due to the relatively narrow field of view and low distortion of the OpNav camera, k_2 and k_3 are not very observable and, despite their fluctuations, their impact on the model is relatively small. Nevertheless, all sets of successful calibrations and associated residuals were deemed acceptable for use in OpNav passes.

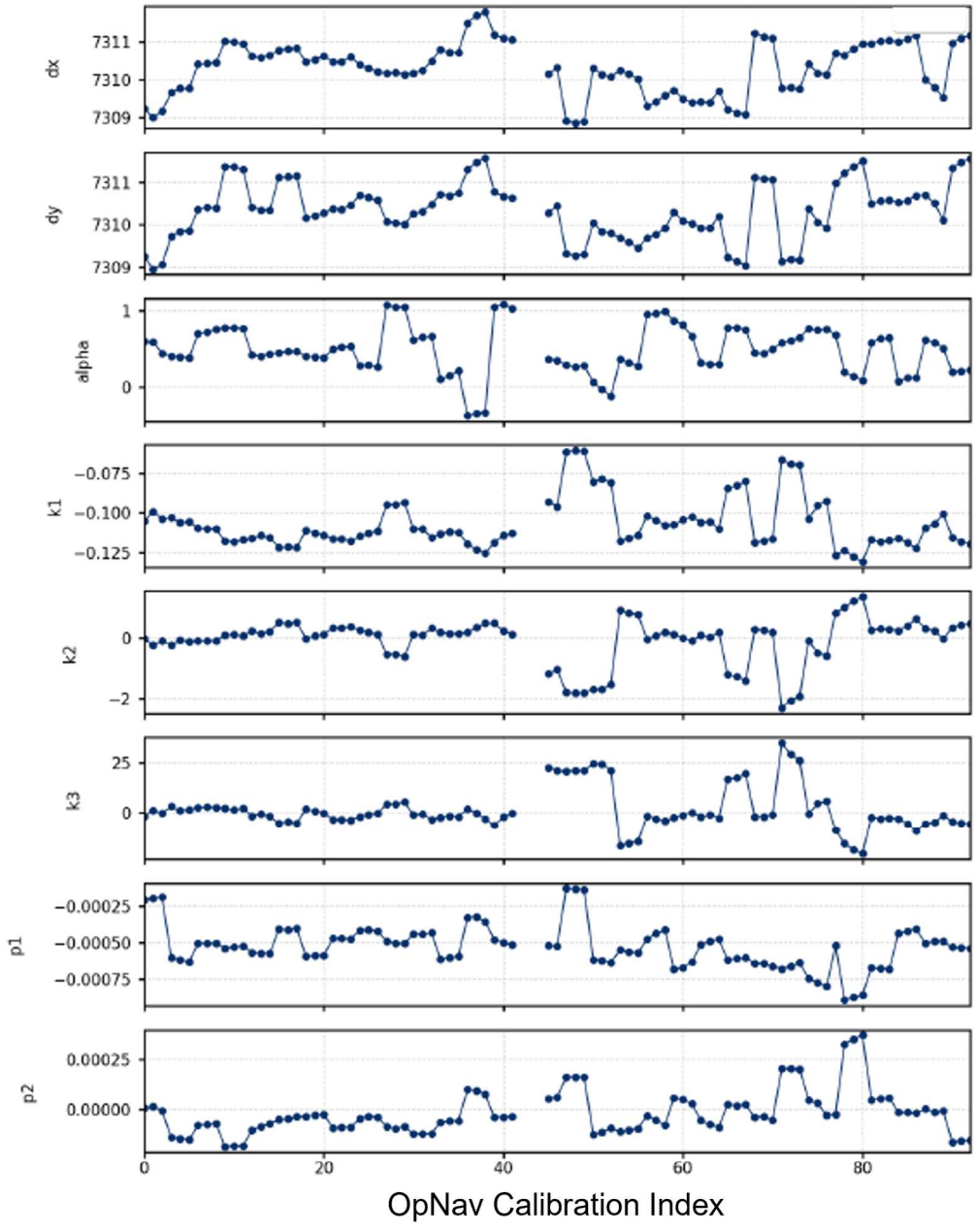

Fig. 4 Summary of OpNav calibration resulting parameters

The system also estimates the relative alignment of the OpNav camera and STs during calibrations. Figure 5 shows the angular change in orientations between the sensors across all calibrations relative to the measured values obtained during ground operations. There is a shift between ground and flight on the order of 100 arcsec for both STs,

but the relative orientations were relatively stable across in-flight measurements. Note that for the calibrations that span index 45-50 occurred with the spacecraft oriented such that the optical bench that both the OpNav sensors and STs are attached to are mounted to were in direct sunlight. There is a larger shift in orientation observed for these calibrations due to thermal effects, but the magnitude of the thermal impact was less than 20 arcsec. Additionally, the calibrations spanning indices 42-50 failed on ST2 due to the sun being directly in the ST field of view, leaving the ST unable to produce attitude solutions. Additionally, calibration interlock angles are unavailable for ST2 on indices 53-55 due to a temporary sensor file misconfiguration that was not fundamental to the OpNav system architecture.

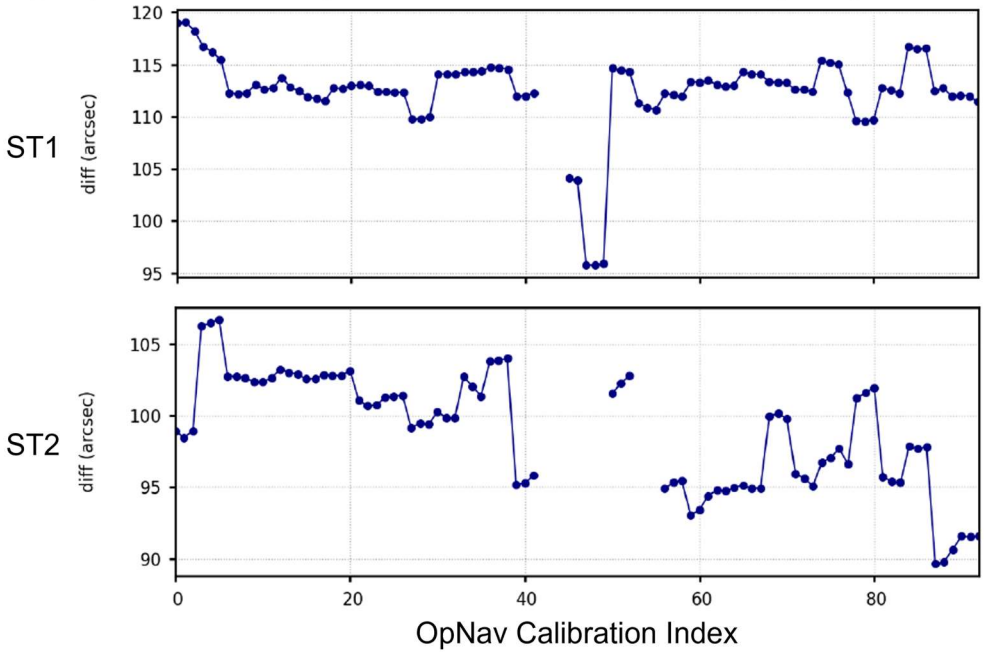

Fig. 5 Summary of OpNav calibration interlock angle changes relative to ground measurements

Overall, OpNav calibration was very successful and demonstrated that there were significant alterations between ground measurements and in-flight measurements, but general sensor stability once the vehicle had reached orbit.

B. Moon Performance

This section details the performance of the OpNav system when observing the Moon, first as a high-level assessment of all Moon passes, and then in more detail for the two certification passes. Figure 6 shows examples of Moon images from Artemis I with the detected limb (blue dots) and reprojected OpNav solution (red circles) overlaid.

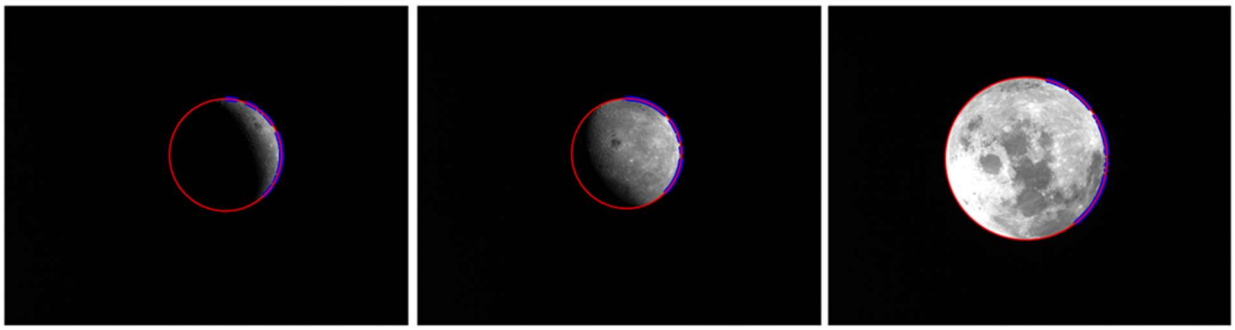

Fig. 6 Detected Limb and Reprojected OpNav Solution overlaid on Moon images

Figure 7 shows the radius residuals (estimate minus BET) for all the Moon passes versus the true range, overlaid with the pre-flight models (3-σ). Negative radius residuals indicate that OpNav was estimating a smaller target radius, meaning over-estimating the range. The Moon radius residuals are in good agreement with the pre-flight expected models. Each pass has a unique bias value, which is due to different regions of the lunar terrain forming the limb. While the radius residuals do present a constant bias throughout a pass, knowledge of the terrain conditions is not carried onboard and, therefore, the bias cannot be easily predicted. As such, the error model was chosen to have a zero bias and the noise increased to encompass all terrain variability. Figure 8 shows the centroid residuals for all Moon passes, overlaid with the pre-flight models (3-σ). The centroid is expressed in the illumination frame – that is, a frame where the x-axis is parallel to the sun direction and the y-axis is perpendicular. Similar to the radius, the centroid residuals have a consistent, unique bias throughout each pass. However, because of the uncertainty in the BET pointing data, we cannot say how much of the centroid bias is due to the algorithm or how much is due to inaccuracies in the BET.

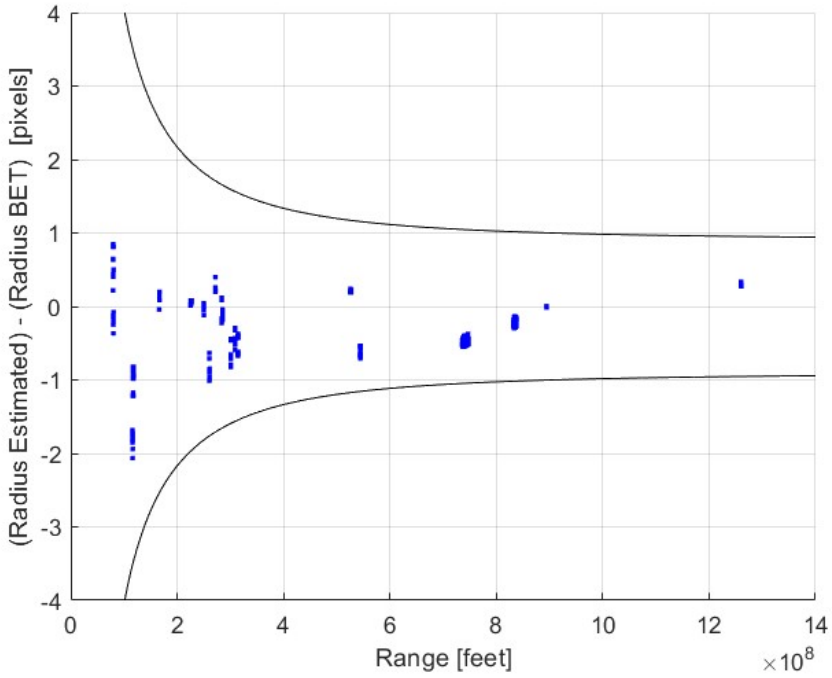

Fig. 7 Moon Radius Residuals for All Passes

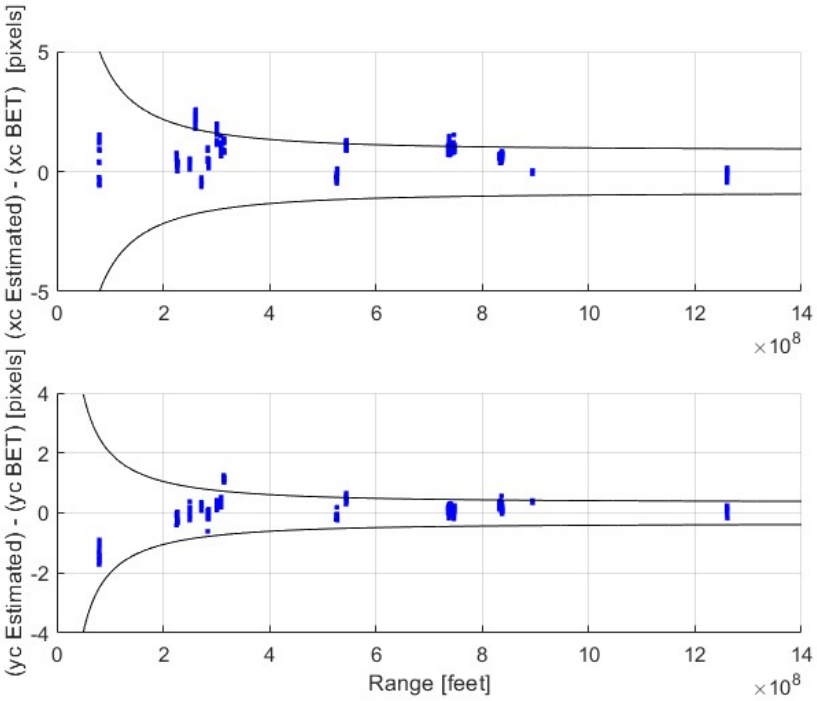

Fig. 8 Moon Centroid Residuals in Illumination Frame for All Passes

1. Moon Certification Pass Details

The onboard uncertainty assessment for the Moon Certification Pass (Pass #3 from Table 1) yielded a range error of ~24kft and a pointing error of 36.2 arcsec. Figure 9 and Fig. 10 show the radius and centroid residuals as compared to the BET (blue dots), overlaid with the pre-flight error bounds (dashed black lines). The range uncertainty is insignificant as compared to the overall range residuals, so we can confidently say the algorithm performed well within the expected error bounds.

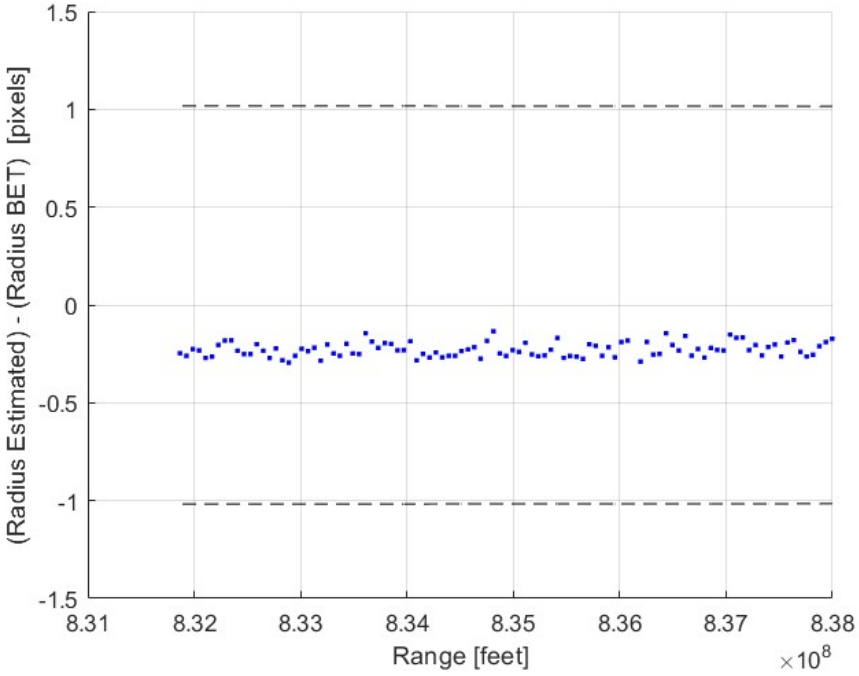

Fig. 9 Moon Certification Pass Radius Residuals

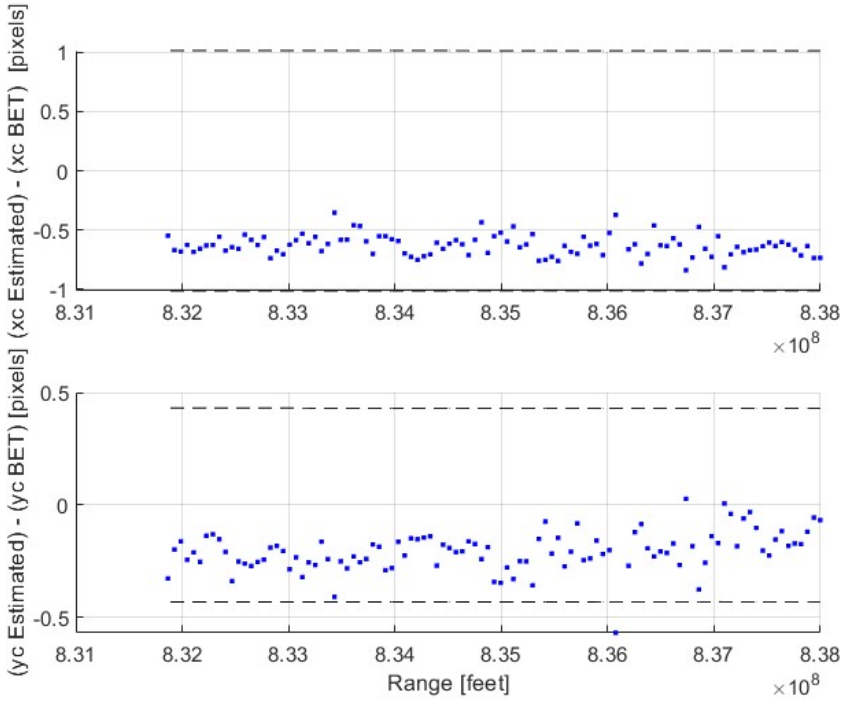

Fig. 10 Moon Certification Pass Centroid Residuals

2. Moon Back-up Certification Pass Details

The onboard uncertainly analysis yielded similar BET errors for the Moon Back-up Certification Pass (Pass #4 from Table 1) (~24kft in range and 36.4 arcsec in pointing). It is notable that the x-direction centroid residuals are closer to

– and, at times, exceed - the error bounds. The pointing uncertainty is non-directional, so we cannot attribute the additional error to a specific axis. Taking into account the 36.4 arcsec pointing uncertainty (which equates to 1.27 pixels), we believe the centroid residuals fall within the expected pre-flight models.

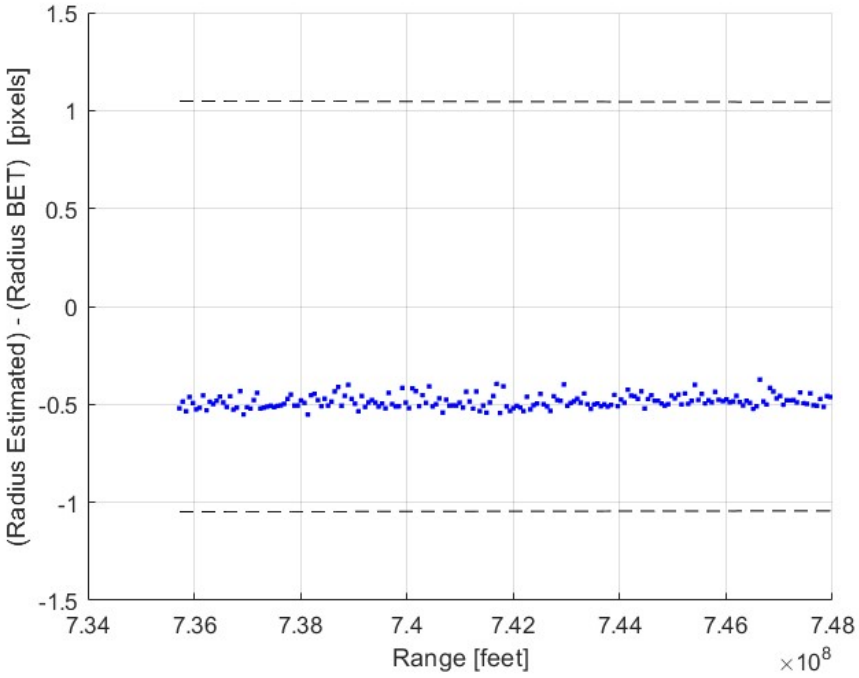

Fig. 11 Moon Back-up Certification Pass Radius Residuals

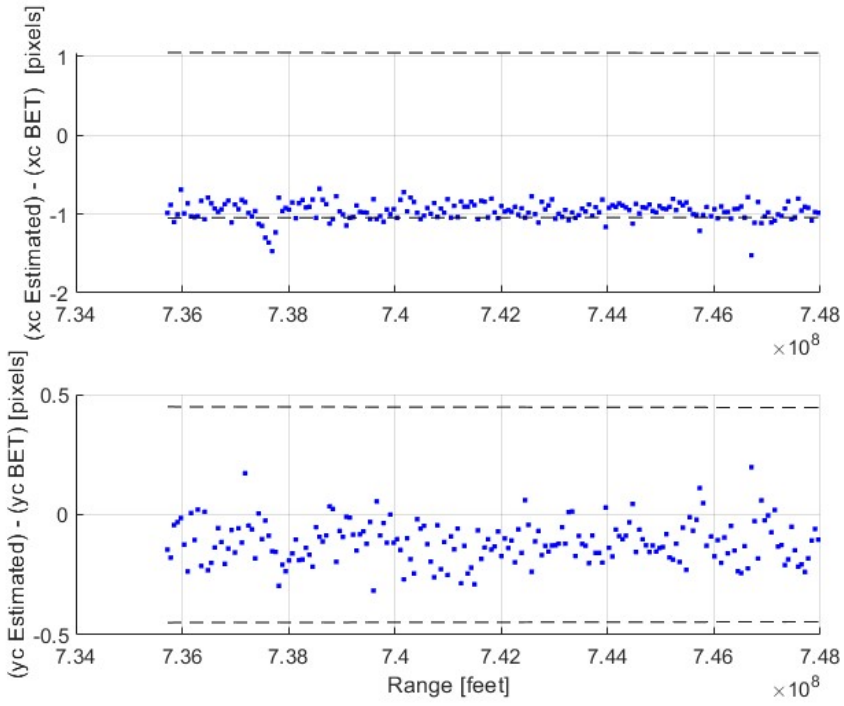

Fig. 12 Moon Back-up Certification Pass Centroid Error

3. *Comparison of Non-Iterative OpNav Algorithms*

Using images from the Moon Certification Pass (Pass #3 from Table 1), we compared the onboard OpNav performance for both the non-iterative and iterative algorithms flown on Artemis I. In Figs. 13-15 show the residuals between the BET and each of the onboard OpNav solutions (left plots) and between the two onboard solutions (right plots). The statistics are summarized in Table 2. When interpreting these data, note that the IFOV of the OpNav camera is 28.2 arcsec and that the pointing knowledge is on the order of 36.4 arcsec (= 1.27 pixel). Also note that the illumination direction is approximately parallel with the x-axis.

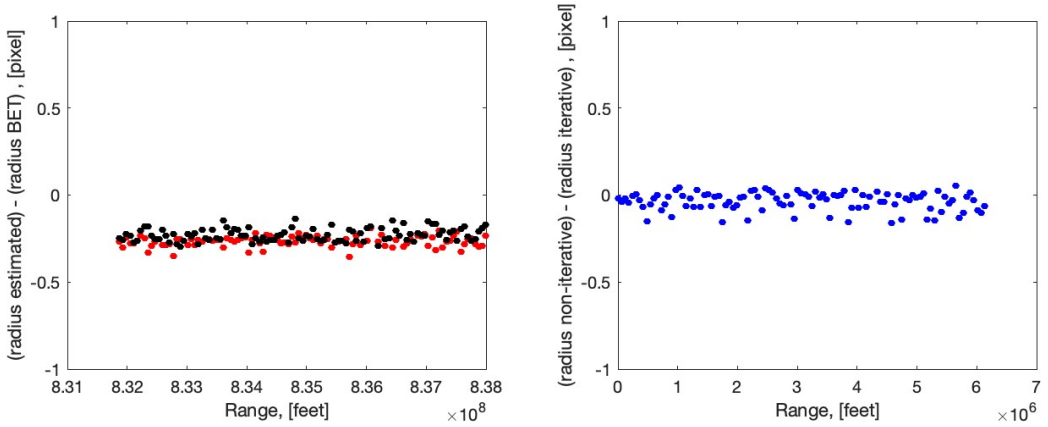

Fig. 13 Comparison of Moon radius residuals for the non-iterative and iterative algorithms on OpNav Pass #3. In the left plot, red is non-iterative (CRA) and black is iterative.

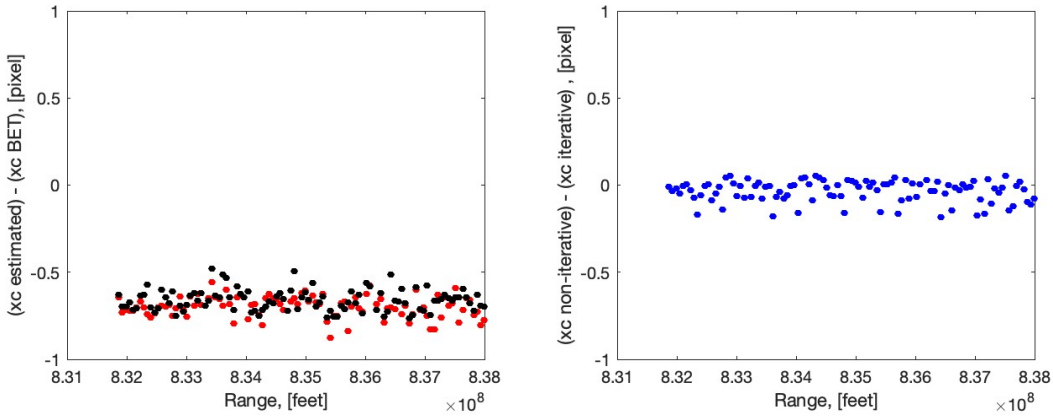

Fig. 14 Comparison of Moon X-centroid residuals for the non-iterative and iterative algorithms on OpNav Pass #3. In the left plot, red is non-iterative (CRA) and black is iterative.

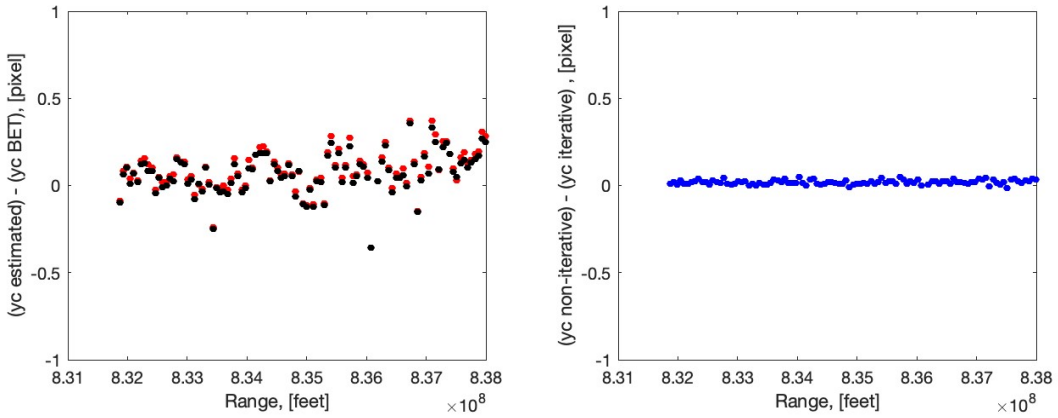

Fig. 15 Comparison of Moon Y-centroid residuals for the non-iterative and iterative algorithms on OpNav Pass #3. In the left plot, red is non-iterative (CRA) and black is iterative.

Table 2 summarizes the statistics for residuals between the onboard OpNav algorithms and the BET for the Moon Certification Pass. All residuals are reported in units of pixels.

Table 2

Parameter	Statistic (pixels)	OpNav image residuals (as compared to BET)		Correlation between non-iterative & iterative residuals
		Non-Iterative	Iterative	
x-direction centroid	Mean	-0.697	-0.661	0.4851
	Standard Deviation	0.060	0.061	
y-direction centroid	Mean	0.086	0.067	0.9946
	Standard Deviation	0.117	0.112	
apparent radius	Mean	-0.265	-0.229	-0.2570
	Standard Deviation	0.030	0.037	

A few things are immediately evident from these data. First, we observe that all residuals (both bias and standard deviation) are subpixel---often substantially so. Second, the standard deviation for both onboard OpNav methods are identical to within a few thousandths of a pixel. This second observation is consistent with what was found when comparing the CRA with the horizon scanning OpNav method used to process Cassini OpNav data [15]. Third, the results are almost identical (near perfect correlation) in the cross-sunlight direction, again consistent with the benchmarking in Ref. [15]. Fourth, and finally, we see some small systematic differences between the two results in the x-direction (along the sunlight direction). The mean discrepancy is on the order of about 0.036 pixels, or about half a standard deviation in the x-direction. However, since the BET pointing knowledge error is ~1.2 pixels (orders of magnitude larger), we have no way of knowing which of these is closer to "truth."

To determine if the differences between the two OpNav algorithms were statistically significant, we performed a two-sample t-test using the 102 measurements shown in Figs. 13-15. Here, we tested the null hypothesis that the two sets of observations (from each of the algorithms) were drawn from the same underlying distribution. In the case of the y-direction centroid, the null hypothesis was accepted (p-value of 0.236). This suggests that differences in the y-direction centroid solutions are not statistically significant. However, in the case of the x-direction centroid and radius, the null hypothesis was rejected (p-values: 3.37×10^{-5} for x-centroid; 2.98×10^{-13} for radius). This suggests that there is a statistically significant difference in the x-centroid and apparent radius estimated by the two OpNav algorithms.

Despite the result of the two-sample t-test, we note that most subpixel localization algorithms suitable for real-time navigation rarely achieve residuals below about 0.07-0.1 pixel---which is more than twice the difference in the means produced by each algorithm. Moreover, this discrepancy is especially small given the comparatively poor pointing knowledge of Orion (about 1.27 pixels). Consequently, while statistically significant, we believe that the discrepancy between these two methods is unlikely to be of significant practical importance in most cases.

In summary, we conclude that the performance of the two onboard OpNav algorithms assessed during the Moon Certification Pass (Pass #3 from Table 1) was similar.

C. Earth Performance

This section details the performance of the OpNav system when observing the Earth. The Earth presented unique challenges for the OpNav system, including: (1) the presence of the atmosphere obscures the limb and the limb detection algorithm actually identifies the edge of the atmosphere and not the true limb, and (2) clouds and the Antarctic ice sheet are very reflective and caused portions of the limb to be over-exposed.

1. Earth Certification Pass Details

The Earth Certification Pass (Pass #1 from Table 1) was the very first time the OpNav system was demonstrated in flight. Figure 16 plots the radius residuals over the course of the 2-hour pass. It is interesting to note the two distinct residual trends. This is attributed to a change in the camera exposure. The initial commanded camera exposure was 200µs, which resulted in very over-exposed images due to the bright clouds and Antarctic ice sheet. The auto-exposure logic drove down the exposure until it reached the hard stop (minimum exposure time) of the camera. The first few data points on the radius plot illustrate how the changing exposure affects the measurement. Eventually the auto-exposure logic toggles the camera between 1µs and 50µs. The change in exposure results in nearly a 0.5 pixel difference in the radius measurement.

An assessment of the ground state update errors was performed to give a rough estimate of 18kft in range error in the onboard state. However, even with the added 18kft of uncertainty (0.01 pixels at this range), this does not account for the high radius residuals seen.

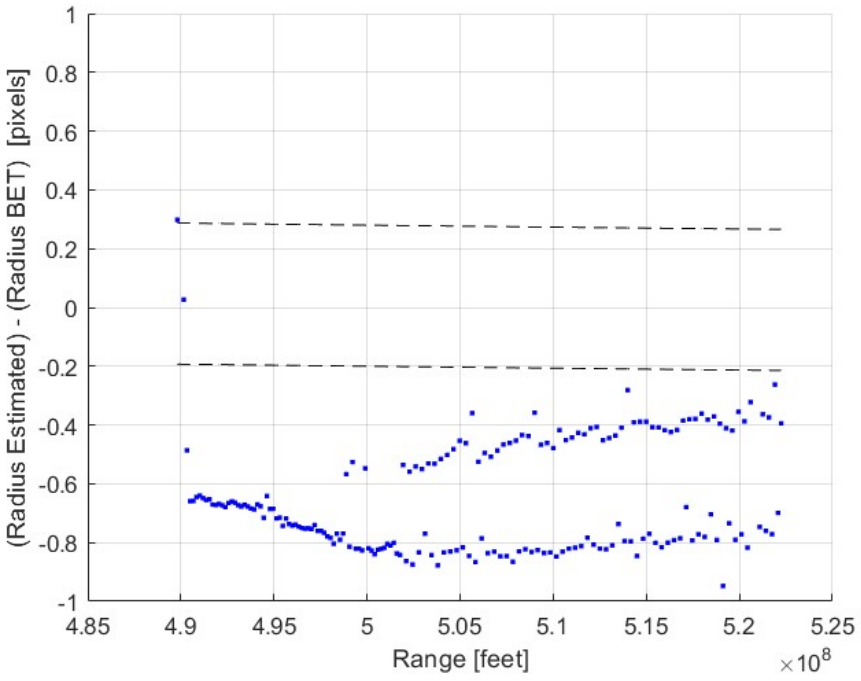

Fig. 16 Earth Certification Pass Radius Residuals

Figure 17 shows the centroid residuals. The uncertainty assessment indicated the onboard pointing error was 7.6 arcsec (0.27 pixels). With the added uncertainty, the centroid residuals mostly stayed in bounds, with several spikes present. Many of the spikes can be attributed to what's referred to as "timetag jitter", in essence the images are

not taken at precisely the stamped time tag. The truth data is taken at the time stamp of the image, so this results in a slight discrepancy when comparing to truth data.

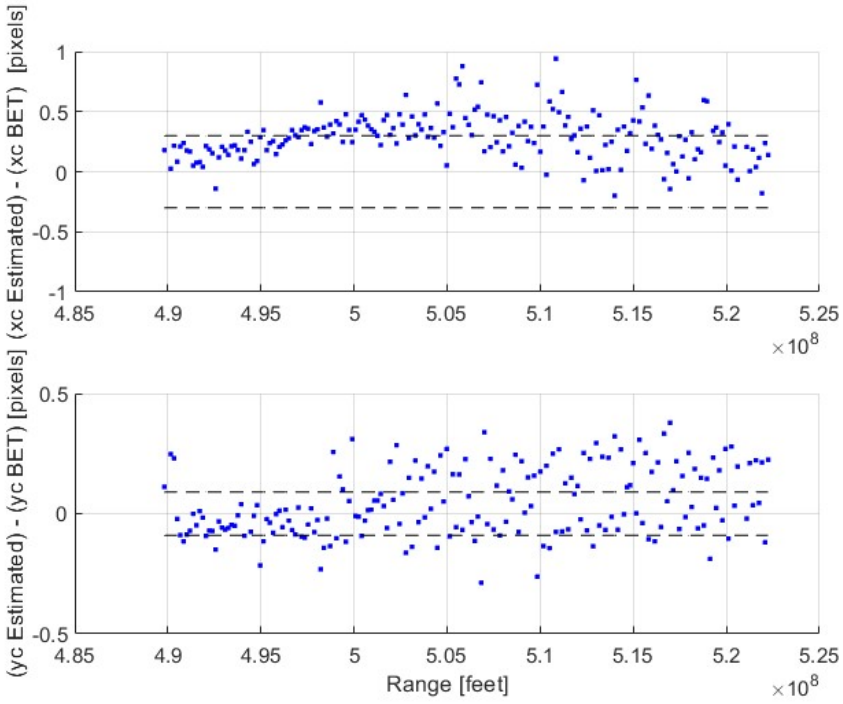

Fig. 17 Earth Certification Pass Centroid Residuals

2. Earth Back-up Certification Pass Details

The back-up certification pass (Pass #2 from Table 1) was the second opportunity to demonstrate the OpNav system capability. The pass functioned similarly to the certification pass, where the initial commanded exposure resulted in saturated images, and the auto-exposure logic drove the exposure down to the hard stop. The exposure toggled throughout the 2-hour pass.

The data follows a similar trend to the Certification Pass: larger than expected negative radius residuals, centroid residuals mostly within the expected bounds + onboard uncertainty, and ~40kft radius bias.

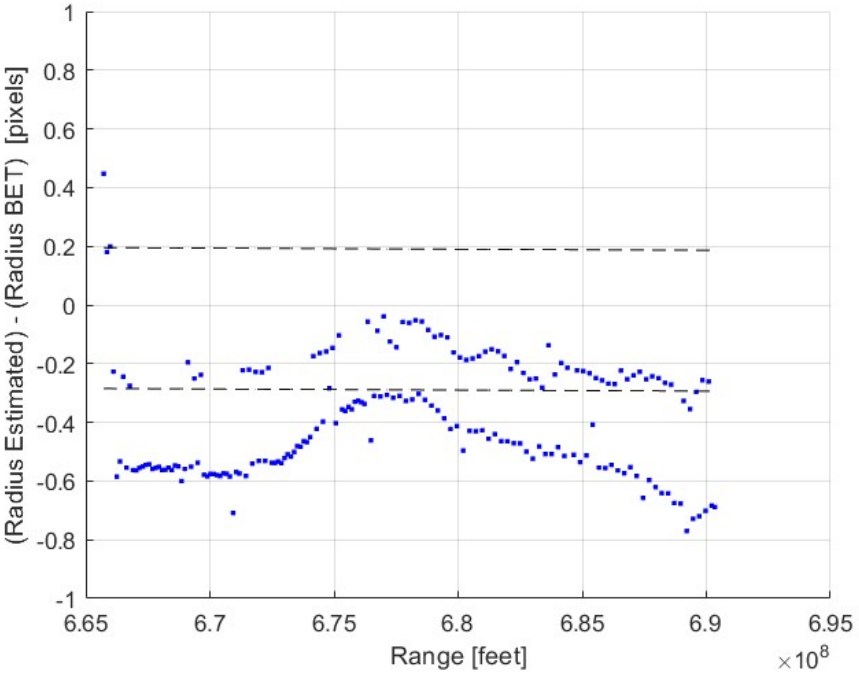

Fig. 18 Earth Back-up Certification Pass Radius Residuals

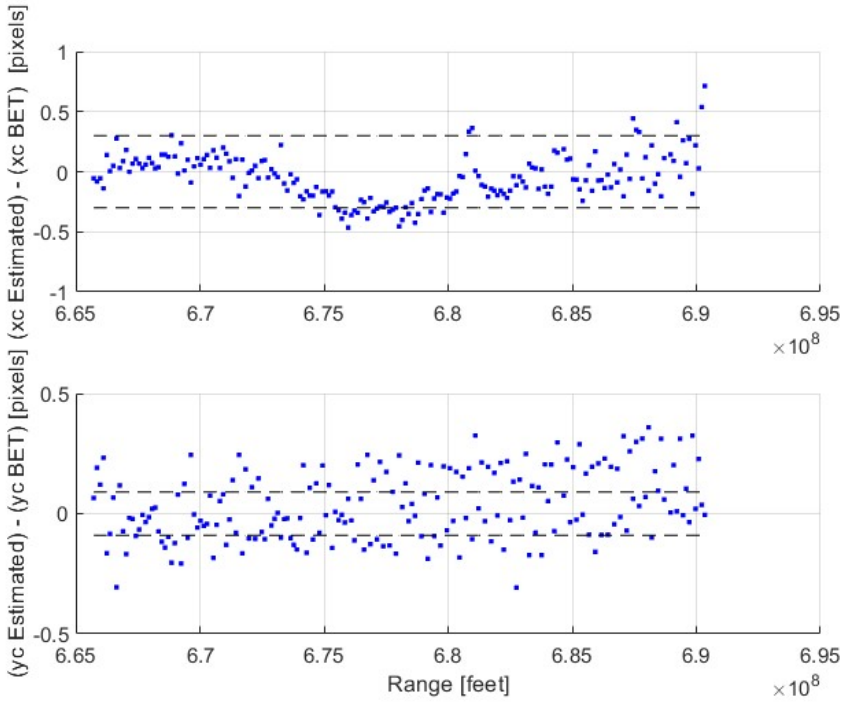

Fig. 19 Earth Back-up Certification Pass Centroid Residuals

3. Earth Atmosphere Bias

Prior to the flight, it was known that the Earth's atmosphere will bias the limb-finding algorithm and the range measurement. To account for this, an atmosphere bias term was added to the Earth's polar and equatorial radii when estimating the range. Tuning of this bias parameter was difficult for two reasons: 1) there is limited Earth imagery with accurate truth data, and 2) the uncertainty of the OpNav camera's detection of the atmosphere. A value of 115kft (35km) was chosen as a reasonable guess at the atmosphere bias.

Figure 20 shows a comparison of the true limb (i.e. the limb that would be produced by an atmosphere-less Earth), the detected limb, and the guess of the limb with the atmosphere bias for one of the properly exposed Earth images from the certification pass. It is evident from this plot that 115kft (35km) is an over-estimation of the atmosphere bias, as the actual detected limb (blue dots) do not line up with the predicted detected limb (red line). The algorithm is detecting the limb further "inside", so when adding the 35km atmosphere bias, the calculated radius is smaller than it should be, resulting in a large range estimate. From this, it is clear that the large radius errors (outside 3-σ) are caused by an incorrect atmosphere bias assumption.

The average offset between the true limb and the detected limb is 1.18 pixels for this image, which equates to 79.5kft (24.25km) of radius difference at a range of 4.9e8ft (1.49e5km). Repeating this same pixel distance calculation for all the images in the certification passes yields an average atmosphere bias of ~82kft (~25km).

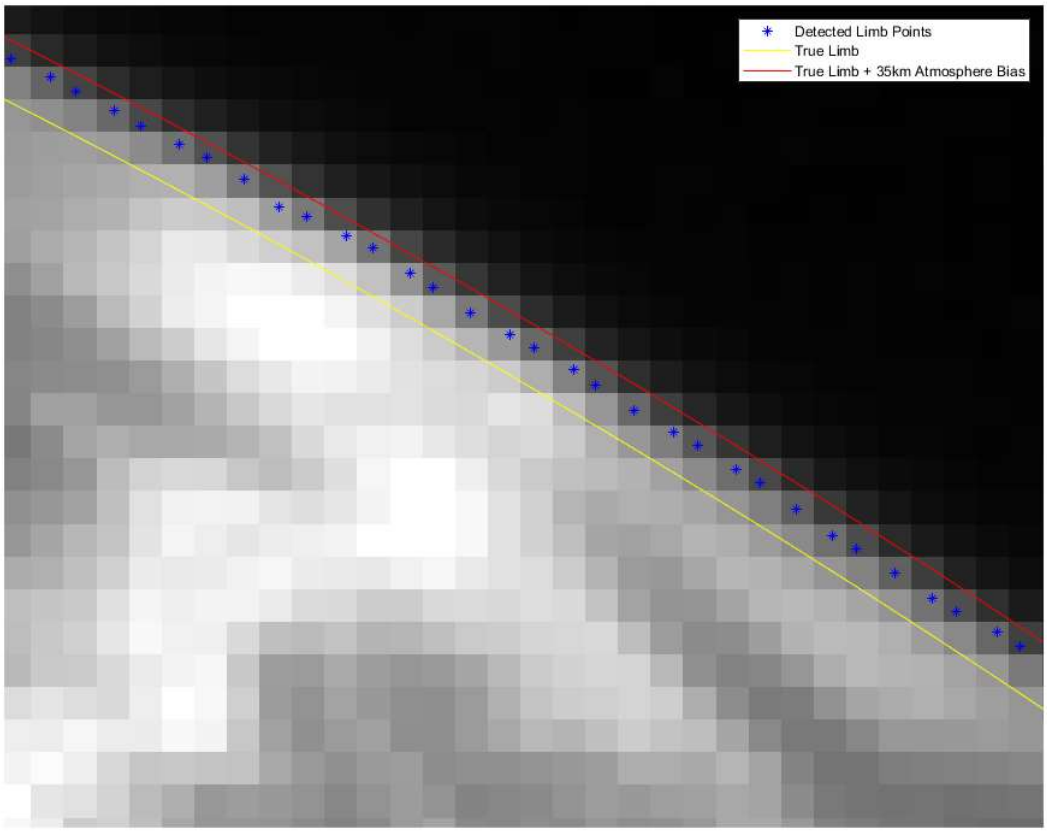

Fig. 20 Earth Atmosphere Bias

An atmosphere bias of 82kft is consistent with what the onboard navigation filter bias state was estimating. At the end of the certification passes, the biases were 39.8kft (12.15km) and 40.3kft (12.3km), respectively. This means that the filter was adjusting the OpNav radius measurements by ~40kft (~12km). Effectively, the filter was estimating the OpNav radius measurements to be ~40kft too small, which is in line with the difference in the pre-flight atmosphere bias 115kft (35km) compared to the 82kft (25km) bias found above (115kft – 40kft = 75kft).

Using the new atmosphere bias of 82kft, the Earth images were re-processed using the offline MATLAB scripts to assess the change in performance. Figure 21 shows the radius error comparison using 82kft bias versus the

flight results using 115kft bias. The new atmosphere bias significantly improved the radius errors as compared to the BET.

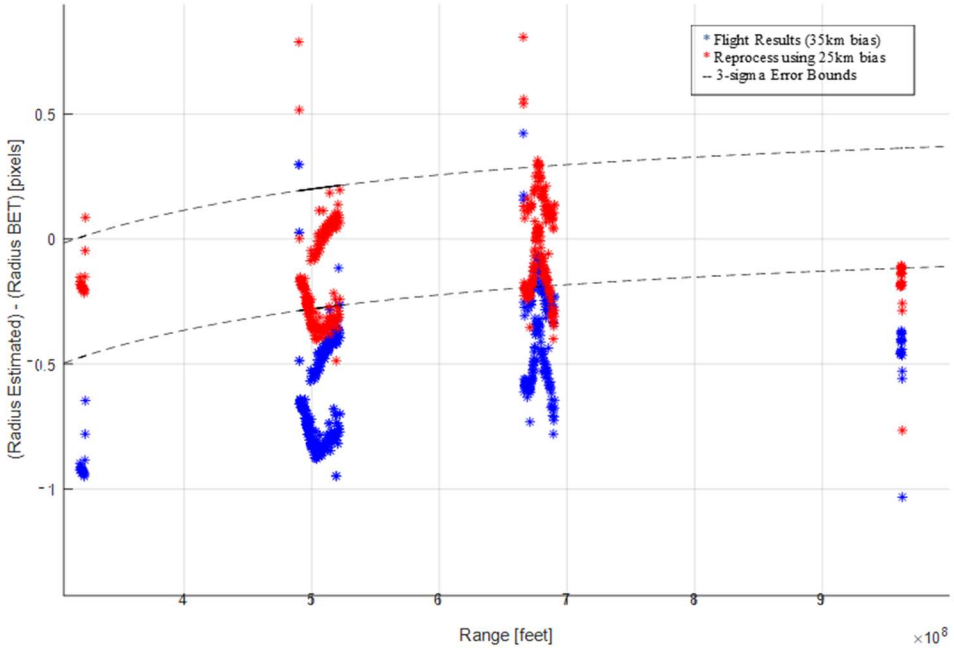

Fig. 21 Radius Residuals Using 25km Atmosphere Bias

V. Conclusions

The Artemis I flight successfully demonstrated (for the first time!) an autonomous, onboard Optical Navigation System. We have made some valuable conclusions that can be taken forward to Artemis II and beyond: (1) Despite an initial shift in the calibration due to the launch conditions, the camera calibration results remained stable throughout the mission. A ground calibration and then an initial on-orbit calibration are necessary, but performing a calibration prior to every pass is not essential. (2) The non-iterative method produced nearly identical results to the iterative method. For memory and CPU savings, the iterative method could be removed for images of the Moon. A comparative study has yet to be performed on Earth images. (3) The OpNav measurements were in very good agreement with the Orion BET, as compared to the pre-flight models. The Earth's atmosphere provided a challenge for the algorithm, as it biased the range measurements more than predicted. Using the results from the Artemis I flight, the error models can be updated to better reflect the actual performance of the OpNav system.

VI. References

[1] Holt, G.N., D'Souza, C.N. and Saley, D. "Orion Optical Navigation Progress Toward Exploration Mission 1," AIAA 2018-1978. *2018 Space Flight Mechanics Meeting*. January 2018.

[2] Holt, G.N., D'Souza, C.N., Wasinger, M., "An Overview of the Artemis I Navigation Performance", *AAS Guidance, Navigation and Control (GN&C) Conference,* Paper AAS 23-057, 2023

[3] Christian, J.A., "A Tutorial on Horizon-Based Optical Navigation and Attitude Determination with Space Imaging Systems," *IEEE Access*, Vol. 9, 2021, pp. 19819-19853. https://doi.org/10.1109/ACCESS.2021.3051914

[4] Christian, J.A., "Accurate Planetary Limb Localization for Image-Based Spacecraft Navigation," *Journal of Spacecraft and Rockets*, Vol. 54, No. 3, 2017, pp 708-730. https://doi.org/10.2514/1.A33692

[5] Owen, W.M., "Methods in Optical Navigation," *AAS/AIAA Space Flight Mechanics Meeting,* Paper AAS 11-215, 2011.

[6] Christian, J.A., "Optical Navigation using Planet's Centroid and Apparent Diameter in Image," *Journal of Guidance, Control, and Dynamics*, Vol. 38, No. 2, 2015, pp. 192-204. https://doi.org/10.2514/1.G000872

[7] Teil, T., Schaub, H., and Kubitschek, D., "Centroid and Apparent Diameter Optical Navigation on Mars Orbit," *Journal of Spacecraft and Rockets*, Vol. 58, No. 4, 2021, pp. . https://doi.org/10.2514/1.A34815

[8] Renshaw, D.T., and Christian, J.A., "Subpixel Localization of Isolated Edges and Streaks in Digital Images," *Journal of Imaging*, Vol. 6, No. 5, 2020. https://doi.org/10.3390/jimaging6050033

[9] Christian, J.A., Benhacine, L., Hikes, J., and D'Souza, C., "Geometric Calibration of the Orion Optical Navigation Camera using Star Field Images," *The Journal of the Astronautical Sciences*, Vol. 63, No. 4, 2016, pp 335-353. https://doi.org/10.1007/s40295-016-0091-3

[10] Christian, J.A., and Robinson, S.B., "Non-Iterative Horizon-Based Optical Navigation by Cholesky Factorization," *Journal of Guidance, Control, and Dynamics*, Vol. 39, No. 12, 2016, pp 2757-2765. https://doi.org/10.2514/1.G000539

[11] Mortari, D., D'Souza, C.N., and Zanetti, R., "Image Processing of Illuminated Ellipsoid," Journal of Spacecraft and Rockets, Vol. 53, No. 3, 2016, pp. 448-456. https://doi.org/10.2514/1.A33342

[12] Samaan, M., Lockhart, S., Holt, G.N., Mamich, H., "On-Ground Calibration and Optical Alignment for the Orion Optical Navigation Camera", *John L. Junkins Dynamical Systems Symposium*, Paper JSC-E-DAA-TN55364, 2018.

[13] Conrady, A.: Decentered lens system. Mon. Not. R. Astron. Soc. 79, 384–390 (1919);

[14] Brown, D.: Decentering distortion of lenses. Photogramm. Eng. 32(3), 444–462 (1966)).

[15] Hollenberg, C., Christian, J.A., Bhaskaran, S., and Owen, W., "Centroiding Performance for Horizon-Based Optical Navigation with Cassini Images of Dione and Rhea," *AAS/AIAA Space Flight Mechanics Meeting*, Paper AAS 19-494, 2019.